Iranian Journal of Medical Physics

ijmp.mums.ac.ir

Design and Fabrication of Optical Bandpass Filters for Safe 222 nm UVC Light Generation in Medical Disinfection Applications

Mohammad Reza Rashidian Vaziri[1], Ali Eskandari[2], Kimia Ghasemi Arzanani[2], Parviz Parvin[2], Samaneh Sharif [3,4*]

1. Department of Physics, Faculty of Sciences, Ferdowsi University, Mashhad, Iran
2. Department of Physics, Amirkabir University of Technology, Tehran, Iran
3. Medical Genetics Research Center, Mashhad University of Medical Sciences, Mashhad, Iran
4. Department of Medical Genetics, Faculty of Medicine, Mashhad University of Medical Sciences, Mashhad, Iran

ARTICLE INFO

Article type:
Original Paper

Article history:
Received: Jan 20, 2026
Accepted: Mar 04, 2026

Keywords:
Medical Disinfection
UVC Light
Bandpass Filters
222 Nm Wavelength
Metal-Dielectric Filters
Al/Mgf₂
Far-UVC
Optical Thin Films

ABSTRACT

Introduction: Recent global pandemics have highlighted the urgent need for effective and safe sterilization technologies. Ultraviolet-C (UVC) radiation at a wavelength of 222 nm has attracted considerable attention due to its strong germicidal efficacy combined with its limited penetration into human tissues. The generation of safe 222 nm UVC light requires optical bandpass filters that selectively transmit this wavelength while suppressing longer, potentially harmful emissions.

Material and Methods: In this study, metal–dielectric optical bandpass filters optimized for 222 nm UVC applications were designed and fabricated. The design process involved a review of previous studies, material selection, and layer thickness optimization using numerical modeling based on the transfer matrix method. Aluminum was employed as the metallic layer and magnesium fluoride as the dielectric material. The filters were fabricated using physical vapor deposition and characterized by UV–Vis spectroscopy. The effects of deposition errors, post-deposition thermal annealing, and laser damage threshold were also investigated.

Results: Several optimized designs for 222 nm optical bandpass filters were obtained, offering flexibility based on material availability and desired spectral characteristics. Experimental results demonstrated peak transmission wavelengths close to 222 nm with acceptable bandwidths for safe UVC applications. Thickness variations in dielectric layers were identified as the dominant factor influencing spectral shifts, while post-deposition thermal annealing was found to degrade filter performance. The laser damage threshold of the fabricated filters was measured to be approximately 1.3 J/cm².

Conclusion: The developed metal–dielectric bandpass filters demonstrate suitable optical performance for generating safe 222 nm UVC radiation. These findings support the development of reliable far-UVC light sources for medical disinfection applications, contributing to safer sterilization technologies in healthcare and public environments.

►*Please cite this article as:*
Rashidian Vaziri MR, Eskandari A, Ghasemi Arzanani K, Parvin P, Sharif S. Design and Fabrication of Optical Bandpass Filters for Safe 222 nm UVC Light Generation in Medical Disinfection Applications. Iran J Med Phys 2026; 23 (1): 46-58. 10.22038/ijmp.2026.94368.2677.

Introduction

Ultraviolet (UV) radiation is a form of electromagnetic radiation with wavelengths shorter than those of visible light. It is invisible to the human eye but can have various effects on living organisms and materials. UV radiation is produced by the sun and is also generated by certain artificial sources, such as excimer lamps (excilamps) (1). UV radiation is commonly divided into three subcategories based on wavelength: UVA (320 to 400 nm), UVB (280 to 320 nm), and UVC (100 to 280 nm). One notable characteristic of UVC radiation is its high energy. This high energy makes UVC effective in breaking molecular bonds, and it is particularly efficient at damaging the genetic material (DNA and RNA) of microorganisms. As a result, UVC radiation is often employed for germicidal purposes, such as in ultraviolet germicidal irradiation (UVGI) systems. These systems use UVC light to disinfect air, water, and surfaces by inactivating or destroying bacteria, viruses, and other pathogens. UVGI systems have been employed in healthcare settings, laboratories, water treatment plants, and other environments where the control of microbial contamination is crucial. It is important to note that, while UVC radiation has germicidal properties, direct exposure to UVC light can be harmful to human skin and eyes. Therefore, precautions must be taken when using UVC devices, and they should be operated in a manner that prevents exposure to humans.

Although UVC radiation spans a range of wavelengths from approximately 100 to 280 nm, when considering UVC for germicidal purposes, the

*Corresponding Author: Tel: +98-9128121907; Email: SharifMSM983@mums.ac.ir

most effective wavelengths fall within the range of 200 to 280 nm. Specifically, the UVC range that is most commonly used for germicidal applications is typically around 254 nm. The 254 nm wavelength is particularly effective because it corresponds to the peak absorbance of DNA and RNA, making it highly efficient at damaging the genetic material of microorganisms (2). This wavelength is commonly used in UVC germicidal lamps and devices designed for disinfection purposes. The 254 nm wavelength is a widely accepted and practical choice for many applications due to its effectiveness and practical considerations in terms of lamp design and efficiency. However, the use of 222 nm UVC radiation, also known as far-UVC light, is considered safer for human exposure compared to the commonly used 254 nm light (3). The safety aspect is primarily attributed to the fact that 222 nm far-UVC light has limited penetration into living tissues and, therefore, is less harmful to human skin and eyes (4). Far-UVC light at 222 nm is absorbed by the outermost layers of the skin and the outer layer of the eye (the cornea). This limited penetration means that it does not reach the deeper layers of the skin or the sensitive internal structures of the eye, reducing the risk of harm to living tissues (5, 6). The limited penetration also means that far-UVC light is less likely to cause damage to the DNA in the nuclei of human cells, as it doesn't reach these critical cellular structures. Despite its limited penetration into living tissues, 222 nm UV light is still effective at inactivating bacteria and viruses (7, 8). It can disrupt the DNA and RNA of microorganisms, rendering them unable to replicate and cause infections (9). Due to its reduced harm to human tissues, there is interest in using 222 nm UV light for continuous disinfection in occupied spaces, such as hospitals, schools, and public areas (10). This contrasts with the use of 254 nm UVC light, which requires precautions to prevent direct human exposure. Welch et al. investigated the use of 222 nm far-UVC light for controlling the spread of airborne-mediated diseases (11). They found that far-UVC light effectively inactivated airborne viruses such as influenza without harm to exposed mammalian skin. The use of continuous low doses of far-UVC light at 222 nm for inactivating airborne viruses has been explored (12). The findings suggested that far-UVC light was effective in reducing the viral load without causing harm to human skin. The effectiveness of 222-nanometer far-UVC light in inactivating airborne SARS-CoV-2, the virus responsible for COVID-19 has been also investigated (13). The researchers found that far-UVC light efficiently inactivated the virus in the air, supporting the potential use of this technology for reducing the risk of airborne transmission. These studies, among others, suggest that 222 nm far-UVC light has promising germicidal properties while being less harmful to human tissues (14).

Optical filters are devices that selectively transmit, absorb, or reflect light of specific wavelengths or ranges of wavelengths while allowing other wavelengths to pass through. These filters are used to control the spectral content of light, influencing the color, intensity, or polarization of the transmitted light. There are several types of optical filters, such as color filters, neutral density filters, polarizing filters, bandpass filters, longpass and shortpass filters among others (15). Optical bandpass filters are a type of optical filter that selectively transmits light within a specific range of wavelengths while blocking or attenuating light outside that range (16). They find applications in various fields, including LiDAR, spectroscopy, and communication and imaging systems (17-19). The key characteristics of optical bandpass filters include their center wavelength (the central or peak wavelength within the transmitted band), bandwidth (the range of wavelengths over which it allows transmission, defined by the full width at half maximum (FWHM)), and optical density (its ability to attenuate light outside the specified band) (20). Bandpass filters can be designed with different technologies, including interference filters that use interference coatings to achieve wavelength selectivity (21). The design of a bandpass filter depends on the specific requirements of the application, such as the desired center wavelength, bandwidth, and optical density.

222 nm UVC light generation involves the use of specific bandpass filters that allow the transmission of 222 nm light for effective sterilization, while blocking harmful longer wavelengths capable of dermal penetration. This can be achieved using a suitably designed far-UVC bandpass filter in front of an excimer lamp, also known as an excilamp (1). Excilamp is a source of UV light based on the spontaneous emission of excimer (exciplex) molecules. The operation of an excilamp is based on the formation of excited dimers (excimers), which spontaneously transition from the excited state to the ground state, resulting in the emission of UV photons. The spectral maximum of excilamp radiation is specified by a working excimer molecule. Krypton-Chloride excimer molecule is mostly used in excilamps for generation of high intensity far-UVC radiations. In studies investigating the biological effects of 222 nm radiation, researchers commonly employ a UV bandpass filter placed in front of the excimer lamp to selectively transmit the dominant 222 nm wavelength while blocking other wavelengths for safety (22-25). A recent study highlighted the crucial role of bandpass filters in mitigating the harmful effects of emissions beyond 222 nm on mouse keratinocytes (26). Specifically, UVC emitted from an unfiltered KrCl lamp led to an increase in cyclobutyl pyrimidine dimer (CPD)-positive cells in the epidermis. In contrast, UVC emitted from a filtered lamp did not significantly elevate CPD-positive cells. Additional studies have

also emphasized the crucial role of bandpass filters in generating safe far UVC light (27-29). Despite the importance of bandpass filters for safe UVC light generation, scientific reports describing their detailed design and fabrication remain limited. Progress in thin-film optics, nonlinear optical phenomena, and radiation measurement techniques has supported the development of advanced optical systems for medical physics and related technologies (30-36). While commercial 222 nm bandpass filters are available for purchase, information regarding their preparation methods remains scarce.

In this paper, we report the design and fabrication of metal-dielectric bandpass filters for generation of safe 222 nm light. Our study explores material selection, layer thickness optimization, and experimental fabrication and characterization. By presenting various optimal designs, we contribute to the development of safe UVC light sources, addressing urgent disinfection needs.

Materials and Methods

Previous Research Overview

UV bandpass filters with narrow bandwidths are generally categorized into three main types: metal-dielectric bandpass filters, all-dielectric bandpass filters, and etalon filters. Metal-dielectric bandpass filters are based on Fabry-Pérot structures. The semi-reflective metal layers, which have high absorption in the visible and infrared regions, prevent light waves at these wavelengths from passing through the filter. The precise location of the Fabry-Pérot resonance peak is achieved by optimizing the structure through material selection and determining their thicknesses. The construction methods for some metal-dielectric bandpass filters for the visible and ultraviolet regions (300-400 nm) have been described in previous reports (37-39). Due to the high optical absorption of metal layers, the Fabry-Pérot structures used are either single or double, and unlike all-dielectric bandpass filters described in the next section, it is not necessary to repeat these structures sequentially to achieve resonance at a specific wavelength. Therefore, the fabrication process of metal-dielectric bandpass filters is simpler, making them more commonly used.

All-dielectric bandpass filters are made from stacks of dielectrics with alternating low and high refractive indices, without using metals in their structure. Due to the interferometric nature of all-dielectric filters, the filter structure exhibits periodic transmission characteristics. This means that a bandpass in the ultraviolet range will always be accompanied by unwanted transmissions in the visible and infrared regions. To eliminate these unwanted bandpass, additional dielectric stacks with different optical parameters must be considered in the filter design, leading to increased structural complexity and higher fabrication costs. Although all-dielectric bandpass filters generally exhibit higher transmission within their operational bandwidth compared to metal-dielectric filters, their application is limited due to the mentioned issue. For more information on the relationships used to describe the performance of this type of filter, refer to reference (21).

Etalon filters are constructed by depositing thin reflective layers on two opposite faces of a rectangular crystal substrate. The cut crystal acts as a substrate on which the reflective layers are deposited. Here too, the multiple reflections of light between the two reflective surfaces inside the crystal lead to the formation of standing waves and resonance at specific frequencies. The major advantage of this type of filter is the reduced impact of surface roughness of the crystal and the resulting scattering effects compared to the other two types of bandpass filters. This is because, in etalon filters, the layers are not stacked sequentially as in the other two types. However, the high cost of growing or procuring crystals with high optical transmission in the required bandwidth, as well as the grinding and polishing of these crystals, limits their applications. More detailed explanations about this type of filter can be found in related references (21, 40, 41).

To comprehensively review the research background, we conducted a search in the Scopus database using the keywords "UV bandpass filter", "Ultraviolet bandpass filter", "bandpass filter for UV", and "bandpass filter for Ultraviolet". Initially, we assessed the relevance of the identified articles by scanning their titles and abstracts. Subsequently, we obtained and thoroughly examined the full texts of the articles that met our criteria. Specifically, we focused on articles discussing the design, construction, or both aspects of UV bandpass filters. Our analysis yielded 12 articles directly relevant to our research, and the results are summarized in Table 1. Additionally, we extracted information related to filter design and construction from these articles, which is also presented in Table 1.

Upon reviewing Table 1, it becomes evident that there are very few articles specifically addressing the design and construction of UV bandpass filters. Notably, none of the sources mention the design and construction of a UV bandpass filter with a central wavelength of 222 nm. In addition to searching the Scopus database, we also conducted a Google search using the same keywords. This search led us to commercial websites that sell UV bandpass filters, as listed in row 13 of Table 1. While these websites confirm the availability of UV bandpass filters across a wide UVC spectrum, including at 222 nm, the information provided is limited to essential details for buyers—such as central wavelength and operational range—without providing insight into the specifics of their design and construction methods.

Table 1. The research background including information sources that mention the design, construction, or both design and construction of UV bandpass filters

Source	Dimensions	Substrate Material	Type of Materials Used	Bandwidth (nm)	Central Wavelength	Type of Filter
(42)	18×19×45 mm^3	-	Crystal Ammonium cobalt nickel sulfate hexahydrate (ACNSH)	450-600	-	Etalon
(43)	220 mm length and 12 mm diameter	-	Crystal Nickel sulphate hexahydrate (NSH)	360-400	-	Etalon
(44)	-	-	Crystal potassium nickel sulfate hexahydrate (KNSH)	Approx. 200-360	-	Etalon
(45)	-	-	Crystals CaF2 and SiO2 coated with polydimethylsiloxane (PDMS)	up to 10	Wavelengths less than 310 nm	Etalon
(46)	Total thickness (0.01±20) µm	Polycarbonate	Metal (silver nanocomposite) and dielectric (polycarbonate)	17–25 for different silver percentages	320 nm	Metal-dielectric
(47)	Metal layer thickness 10 nm - Dielectric layer thickness 50 nm	-	Metal (aluminum) and dielectric (SiO_2)	28	252 nm (for normal incidence and double repetition of structure)	Metal-dielectric
(48)	20 nm thickness aluminum nanogrid with 190 nm period, 30 nm line width, and 250 nm depth	Fused silica	Metal (aluminum nanogrid) and dielectric (SiO_2)	250 - 350	290 nm	Metal-dielectric
(49)	Different thicknesses as per Table 1	Sapphire	SiO_2 and Si_3N_4	30 - 45	For various fabricated samples from 310 to 370 nm	All-dielectric band-pass filter
(50)	Different thicknesses as per Table 1	-	SiO_2 and Si_3N_4	-	240-280 nm	All-dielectric band-pass filter
(51)	Different thicknesses as per Table 2	Fused silica	$Al2O_3$ and SiO_2	4.8	214 nm	All-dielectric band-pass filter
(52)	Different depending on the design	-	TiO_2 and SiO_2	0.47	364.7 nm	All-dielectric band-pass filter
(53-56)	Variable	Variable	Variable	Variable	Variable	Commercial samples

As previously discussed, metal-dielectric bandpass filters present fewer technical challenges during manufacturing and have lower production costs compared to other filter types. Consequently, for commercial applications—such as the production of safe UV radiation devices—these filters are the preferred choice. We have also utilized this type of filter in our study.

Filter Design

This section addresses the theoretical methods required for designing 222 nm bandpass filters. The transfer matrix method is used to calculate the characteristics of multilayered optical filters (57). The transfer matrix method is only capable of calculating the optical transmission spectrum for a structure with predetermined materials and thicknesses. However, a filter designer must also be able to reverse this process; meaning they should determine the type of materials and their thicknesses based on the desired spectral transmission of the filter. An analytical formulation of the inverse transfer matrix that relates the target spectral performance to the layered structure is not feasible. To create a filter design that meets the desired spectral performance with layer specifications, optimization methods must be used. Optimization algorithms frequently employ the transfer matrix method. The optimization process starts with an initial design. The optical transmission spectrum of this initial design is computed for the desired wavelengths and then compared with the target transmission spectrum. Based on the difference between the target spectrum and the computed spectral performance, an error function is generated. This error function is used to adjust the layer structure, and the process of calculating the transmission spectrum is repeated. The optimization process continues until the error between the target spectrum and the computed performance spectrum reaches an acceptable level. Two commonly used optimization algorithms in filter design are genetic algorithms and simplex methods (21).

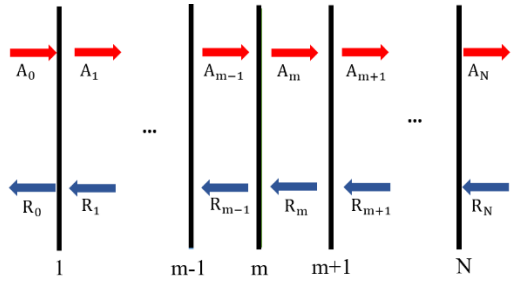

Figure 1. The amplitudes of the forward and reflecting waves, A and R in a multilayer structure. The multilayer structure consists of N+1 layers with different refractive indices and several interfaces (N).

By arranging multiple thin layers of different materials on substrates, the properties of the filter can be optimized for specific optical applications. The properties of filters made from multiple thin layer arrangements can be described based on constructive and destructive interference and reflection and transmission at each interface. The transfer matrix method is used to calculate the reflection and transmission characteristics of light at the required wavelengths. This method uses the conditions of electromagnetic field continuity. For each layer, the corresponding transfer matrix is created. These matrices describe the relationship between the electric fields at the input and output of each layer. By multiplying the transfer matrices of each layer, the overall transfer matrix of the optical filter is obtained. This matrix determines the final characteristics of the filter. Considering a multilayer consisting of a total of *N* layers (see Figure 1), the field amplitudes in layer *m* is calculated using the following relationship (58):

$$\begin{pmatrix} A_m \\ R_m \end{pmatrix} = t_{m-1} \begin{pmatrix} e^{i\delta_{m-1}} & -r_{m-1,m}e^{i\delta_{m-1}} \\ -r_{m-1,m}e^{i\delta_{m-1}} & e^{i\delta_{m-1}} \end{pmatrix} \begin{pmatrix} A_{m-1} \\ R_{m-1} \end{pmatrix} \quad (1)$$

The phase shift is given by $\delta_{m-1} = 2\pi k n_{m-1} d_{m-1}$. d_{m-1} and n_{m-1} represent the thickness and the refractive index of layer *m*-1, respectively, and *k* is the wavenumber. n_{m-1} is the refractive index of layer *m*-1, and dm_{m-1} shows its thickness. A_m and R_m represent the forward and backward travelling electric fields. Moreover, t_{m-1} and $r_{m-1,m}$ are the transmission and the reflection coefficients between interfaces *m*-1 and *m*. The total transfer matrix of the system can be simplified in the following form:

$$\begin{pmatrix} A_N \\ R_N \end{pmatrix} = \frac{1}{T_{11}T_{22} - T_{12}T_{21}} \begin{pmatrix} T_{22} & -T_{12} \\ -T_{21} & T_{11} \end{pmatrix} \begin{pmatrix} A_0 \\ R_0 \end{pmatrix} \quad (2)$$

The net reflection coefficient of a multilayer structure can be determined by calculating the ratio of T_{21}/T_{11}, expressed as $r = T_{21}/T_{11}$. Similarly, the net transmission coefficient can be obtained as $t = 1/T_{11}$ (58, 59). The Essential Macleod software was utilized to determine the optimal thicknesses and the transmission properties of the multilayer structures (60). All simulations assumed normal incidence of the optical field, as indicated by the arrows in Figure 2.

Results

Simulation Results

In this study, multilayer metal-dielectric bandpass optical filters have been designed. Dielectric materials such as MgF_2, LaF_3, SiO_2, and ThF_4 were considered in our simulations due to their widespread use in UV optical coatings (61). When selecting metal materials for metal-dielectric filters, the position of the metal's plasmonic absorption peak plays a crucial role. Aluminum and silver, with absorption peaks at 83 nm and 320 nm, respectively, are potential candidates for 222 nm bandpass filters (38, 62). However, aluminum, with a plasmonic absorption wavelength of 83 nm and further distance from 222 nm, is a better choice. High-purity aluminum is also more cost-effective than pure silver, reducing manufacturing expenses.

Among the simulated dielectric materials (MgF_2, SiO_2, LaF_3, ThF_4), MgF_2 was selected for experimental fabrication due to its superior combination of properties for 222 nm far-UVC applications. MgF_2 exhibits excellent transparency in the deep ultraviolet (transmission extending to ~115 nm with negligible absorption at 222 nm, $k \approx 0$), a low refractive index ($n \approx 1.42$) that provides optimal index contrast with aluminum for efficient Fabry-Pérot resonance, and proven compatibility as a protective overcoat on Al layers to prevent oxidation while maintaining high performance in UV stacks. Compared to alternatives, SiO_2 shows higher absorption below ~250 nm, while LaF_3 and ThF_4, although viable, offer less established deposition protocols, higher cost, or potential handling challenges (e.g., ThF_4 radioactivity concerns). Additionally, MgF_2's mechanical hardness (the highest among common fluorides) and thermal stability during PVD deposition make it practical and reliable for producing durable filters suitable for medical disinfection devices.

The skin depth, a characteristic of metals, represents the penetration depth of light into a material. It is defined as the distance over which the incident light intensity inside the metal decreases to 1/e (approximately 37%) of its original value at the surface. The skin depth can be expressed in terms of light wavelength λ, and the imaginary component of the refractive index *k*, as shown below (63):

$$SD = \frac{\lambda}{4\pi k} \quad (3)$$

Here, λ represents the wavelength of light. For aluminum at 222 nm, the value of k is approximately 1.99 (64). Using this value, the skin depth at 222 nm is approximately 8.9 nm. It's important to note that at higher wavelengths, due to an increase in k (64), the skin depth will be even smaller. Therefore, when designing a 222 nm bandpass optical filter, selecting a single aluminum layer thicker than 8.9 nm ensures minimal transmission in the visible wavelength range.

The initial designs were based on a quarter wave/half wave/quarter wave structure, and the optimal thicknesses for the bandpass filters were calculated using the Essential Macleod software. Figures 2 and 3 depict the optimal designs for 222 nm bandpass filters and their

corresponding transmittances, respectively. In all designs, aluminum (Al) serves as the metal layer, while quartz glass acts as the substrate due to its low UV absorption (65). Given the practical sensitivity of metal layers to scratches and damage from minimal contact, an additional dielectric layer is used as a protective coating atop the designs.

The maximum transmittance for all designs occurs at 222 nm. Other critical design characteristics, such as the FWHM and peak transmittance, are summarized in Table 2. Notably, increasing the peak transmittance is desirable, but it comes at the cost of a larger FWHM. Larger FWHM values result in transmission of unsafe UVC wavelengths, which should be avoided.

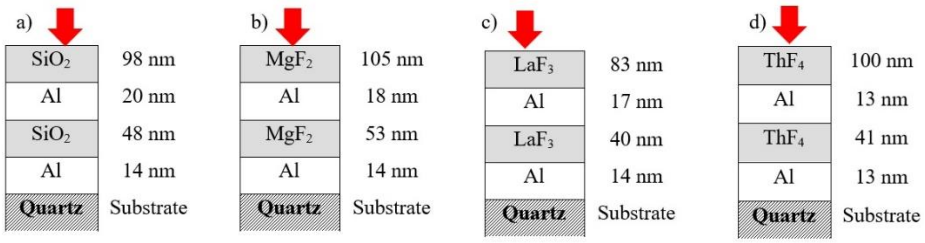

Figure 2. The optimal designs for 222 nm bandpass filters with Al as metal and a) SiO_2, b) MgF_2, c) LaF_3, and ThF_4 as the dielectrics. The arrows indicate the incidence direction of the optical field on the top surface of the filters.

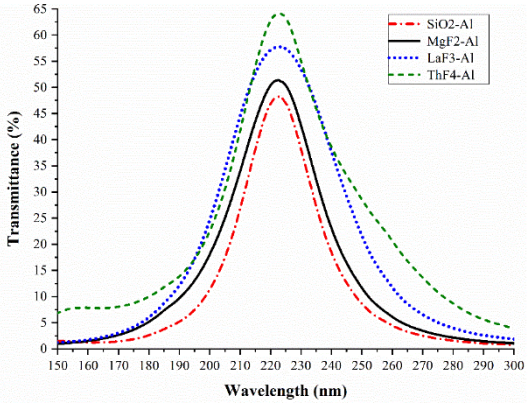

Figure 3. The optical transmittance of the optimal designs for 222 nm bandpass filters.

Table 2. Characteristics of the designed metal-dielectric bandpass filters.

Dielectric	SiO_2	MgF_2	LaF_3	ThF_4
FWHM (nm)	27	33	42	40
Peak transmittance (%)	48	51	57	64
Peak Wavelength (nm)	222	222	222	222

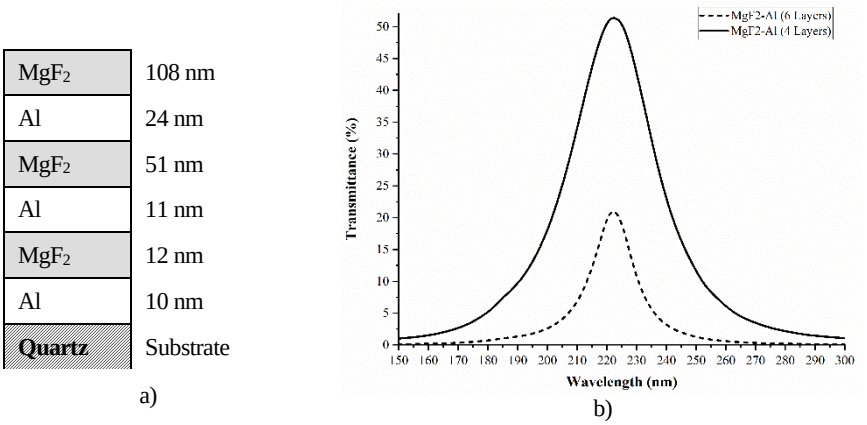

Figure 4. a) The optimal design for a six layer (three periods) Al/MgF_2 bandpass filter and b) its optical transmittance. The optical transmittance of the four layer filter is also shown for comparison.

This paper presents various optimal designs for 222 nm optical bandpass filters, offering users a range of choices. Based on material availability and desired filter characteristics, users can select one of the optimal designs shown in Figure 3. Our focus in this work was on fabricating Al/MgF_2 bandpass filters, and subsequent sections provide results specific to this filter type.

Previously mentioned, due to the high optical absorption of metal layers, metal-dielectric bandpass filters are fabricated either with single or double periodicities. Increasing the periodicity significantly reduces peak transmittance, as typically shown for Al/MgF_2 bandpass filters in Figure 4. Specifically, the peak transmittance decreased from 51% to 21%, and the FWHM narrowed from 33 nm to 17 nm.

Experimental Results

In this work, the polished quartz glass substrates were selected for sequential layer deposition and band-pass filter fabrication. Figure 5 displays the optical transmission spectrum of the prepared quartz glass substrates, measured using a UV-Vis spectrophotometer (Varian Cary 5000). Notably, transmission in the visible region exceeds 90%, while the optical transmission at the working wavelength of 222 nm for the band-pass filter reaches approximately 66%.

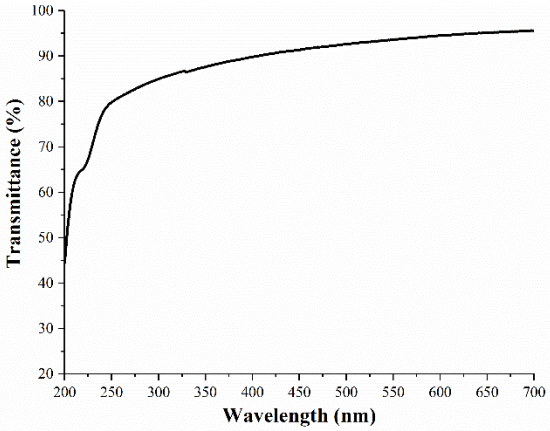

Figure 5. Optical transmission spectrum of the quartz substrate prepared for layer deposition.

Figure 6 presents an Atomic Force Microscope (AFM) image of the surface of one of the quartz glass samples, revealing a measured surface roughness of approximately 0.5 nm. The surface quality of the quartz substrates appears suitable for subsequent multilayer deposition.

Before initiating the deposition process, thorough surface cleaning is essential. The quartz substrates were immersed in a chromic-sulfuric solution and sonicated for 20 minutes. Subsequently, the substrates underwent sonication in a 1:1 solution of hydrochloric acid and distilled water for an additional 20 minutes. Finally, the substrates were rinsed with distilled water and dried in an oven at 45 °C.

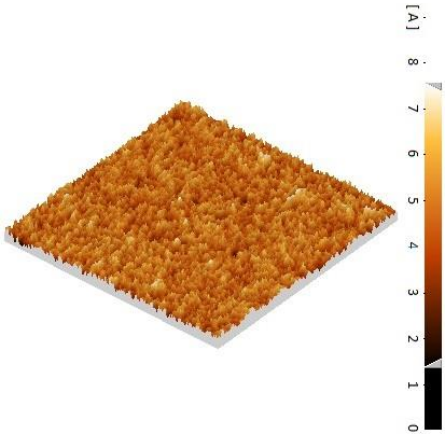

Figure 6. Atomic Force Microscope (AFM) image of the polished quartz glass surface.

For material deposition and bandpass filter fabrication, a physical vapor deposition system manufactured by Balzers, UK (model BAK 760) was employed. Inside the deposition chamber, the pressure was reduced to 5×10^{-5} Torr, and the deposition rate was maintained at 1 nm s^{-1}. The substrate was maintained at room temperature (approximately 25°C) during the deposition process to minimize aluminum roughening while ensuring stable MgF_2 film formation. High-purity aluminum (99.99%) was placed in one crucible, while MgF_2 was placed in another. The layers were deposited on the prepared quartz substrates following the sequence shown in Figure 2b. During deposition, we monitored layer thickness using a quartz crystal microbalance. After completing the deposition process, the chamber door was left closed for one working day to prevent thermal shock and damage to the deposited layers. Finally, the filters were carefully removed from the chamber.

The optical transmission spectrum of the first fabricated bandpass filter sample was measured using UV-Vis spectroscopy, as depicted in Figure 7. According to the measured spectrum, the transmission peak occurred at 247 nm, with a peak transmittance of 41% and a FWHM of 54 nm. Notably, these obtained values considerably deviate from the initially calculated values, as indicated in Table 2.

The observed discrepancies stem from errors encountered during the transition from the design to the fabrication phase of the filter. The primary source of error likely arises from differences between the thicknesses specified during the design phase (as shown in Figure 2b) and the actual thicknesses achieved during layer deposition using the deposition system. Previous experience with the same deposition system suggests that such discrepancies often result from inaccuracies in measuring layer thickness. Quartz crystal microbalances installed in deposition systems require careful recalibration after prolonged use and replacement when they reach the end of their service life.

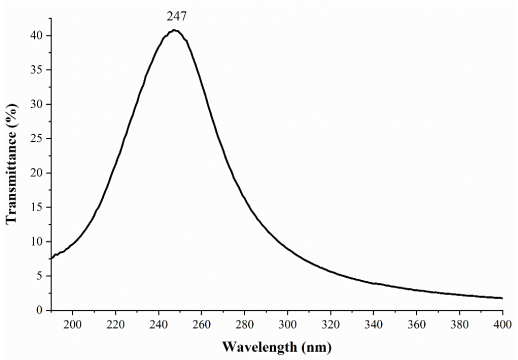

Figure 7. The optical transmission spectrum of the first sample of the Al/MgF_2 bandpass filter. The number above the curve indicates the peak wavelength of the filter in nm.

To mitigate errors arising from thickness measurements, an economical solution involves error modeling. Using the McLeod software, the optical transmission spectrum of the optimized filter (Figure 2b) was modeled by varying the thicknesses of the Al and MgF_2 layers. Assuming a potential error of 5 nm in thickness, we calculated the spectral output separately for the Al layers and the MgF_2 layers.

In Figure 8a, the potential occurrence of a ±5 nm error in the thickness of the Al layers within the optimal design of Figure 2b is examined focusing on the transmitted spectrum output of the bandpass filter. The results reveal that an increase in Al layer thickness relative to the optimal values leads to reduced peak transmittance and FWHM. Considering the thin skin depth of 8.9 nm for Al at a wavelength of 222 nm, this reduction in peak transmittance intensity is understandable. Figure 8b explores the impact of a ±5 nm error in the thickness of the MgF_2 layers within the optimal design of Figure 2b on the transmission spectrum of the bandpass filter. As shown, decreasing the thickness of the dielectric MgF_2 layers results in a significant shift of the peak transmission wavelength toward shorter wavelengths. Comparing Figures 8a and 8b, we conclude that a 5 nm reduction in Al layer thickness causes only a 2 nm shift of the peak wavelength toward shorter values. In contrast, a 5 nm reduction in MgF_2 layer thickness results in a shift of approximately 16 nm. Based on these modeling results, we attributed the increase in the maximum transmission wavelength of the first sample (compared to 222 nm) to a potential error during the deposition of the MgF_2 layers.

To further quantify fabrication tolerances, we performed a linear sensitivity analysis around the optimal design (Al/MgF_2 structure in Figure 2b). From the modeled spectra in Figure 8, the peak wavelength shift is approximately linear for small deviations. A ±1 nm error in MgF_2 layer thickness results in a peak wavelength shift of approximately ±3.2 nm (dominant effect, primarily due to changes in the optical path length of the dielectric layers). In contrast, a ±1 nm error in Al layer thickness causes a much smaller shift of approximately ±0.4 nm, with the primary impact being a reduction in peak transmittance due to increased absorption/scattering in thicker metal layers.

While thickness errors, particularly in the MgF_2 dielectric layers, are the dominant cause of the observed red-shift in the first sample (peak at 247 nm vs designed 222 nm), we also considered potential contributions from deviations in the effective refractive index of the deposited films. In physical vapor deposition of MgF_2 at room temperature (as used here), films can exhibit porosity due to limited adatom mobility, leading to packing densities of 0.72–0.95 and effective refractive indices lower than bulk values (typically n ≈ 1.32–1.38 at UV/visible wavelengths, compared to literature simulation values of ~1.42). Lower effective n would reduce the optical path length (n·d), favoring a blue-shift in the resonance peak—opposite to the observed red-shift. However, adsorption of atmospheric moisture into pores can temporarily increase effective n (water n ≈ 1.33), potentially contributing a minor red-shift component (estimated <5 nm based on typical porosity effects in evaporated MgF_2).

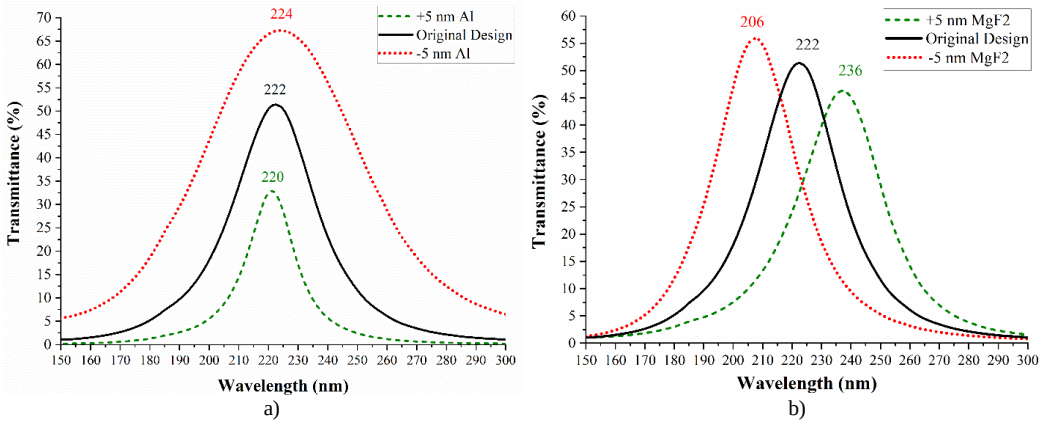

a) b)

Figure 8. Investigation of errors in the thickness of a) Al, and b) MgF_2 during the deposition process on the optical transmittance of the bandpass filter. The dashed and dotted lines represent the effects of +5 nm and -5 nm deposition errors, respectively. The numbers above the curves indicate the peak wavelengths of the filters in nm.

According to Figure 8, the reduction of peak wavelength to bring it closer to 222 nm necessitates decreasing the thickness of the MgF_2 layers. Due to uncertainties regarding the accuracy of the thickness gauge, we achieved this reduction by adjusting the deposition time. Specifically, for the first sample, the deposition time for a 53 nm MgF_2 layer was approximately 7 minutes, while the 105 nm layer required approximately twice that time. In the fabrication of the second bandpass filter (sample 2), the same deposition conditions as for the first sample were maintained but the deposition time for these layers was reduced by 1 and 2 minutes, respectively. After exiting the deposition system, the optical transmission spectrum of the second sample was measured using UV-visible spectrometry (see Figure 9).

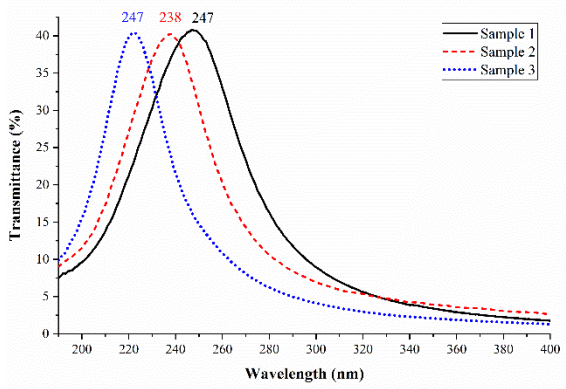

Figure 9. Optical transmission spectra of the first to third samples of the bandpass filters. The numbers above the curves indicate the peak wavelengths of the filters in nm.

As predicted by our modeling, the reduction in MgF_2 layer thickness shifted the peak transmission wavelength of the filter toward shorter values. For the second sample, the peak transmission occurs at 238 nm, with a peak transmission of 40% and a full-width half maximum (FWHM) of 46 nm. To compare the characteristics of the second sample with those from the design phase, Table 3 presents these specifications. Despite the reduction in peak transmission wavelength, it remains far from 222 nm, indicating the need for further reduction in MgF_2 layer thickness.

Table 3. Comparison of the characteristics of samples one to three with the characteristics obtained in the design phase.

	FWHM (nm)	Peak Intensity (%)	Peak Wavelength (nm)
Designed Sample	26	51.4	222
First Sample	54	41	247
Second Sample	46	40	238
Third Sample	37	40.5	223

For the third sample, we maintained the same deposition conditions as for the first and second samples but reduced the deposition time for MgF_2 layers by 2 and 4 minutes (relative to the deposition times of the first sample), respectively. As verified in Figure 9, the peak transmission wavelength of the third filter sample shifted even further toward shorter wavelengths. The peak transmission of the third sample occurs at 223 nm, with a peak transmission of 40.5% and an FWHM of 37 nm. With the continued reduction in MgF_2 dielectric layer thickness, the peak optical transmittance aligns more closely with the 222 nm wavelength. The third sample was considered as the final best sample and further reduction of the MgF_2 layer thickness was ceased.

Post thermal annealing of multilayered samples is a well-known technique for enhancing their structural and optical properties (66). During physical vapor deposition, atoms and ions may not settle into their proper crystalline positions upon cooling and solidification on the substrate, resulting in various crystalline defects. By subjecting the samples to thermal annealing at high temperatures after removing the layers from the deposition apparatus, the kinetic energy of particles within the solid-state layer structure increases, potentially correcting these structural defects. Notably, there have been reports on post-thermal-annealing effects on optical filters and their peak transmittance wavelength shift (67, 68). To explore this idea, one of the second samples was subjected to thermal annealing at 400 degrees Celsius for varying durations in the oven. The choice of 400 degrees Celsius aligns with previous references that used temperatures between 400 and 600 degrees Celsius for this purpose (67, 68). Figure 10 shows the optical transmittance of the second sample after 15, 35, and 45 minutes thermal annealing at 400 degrees Celsius. Surprisingly, thermal annealing did not shift the peak wavelength; instead, it worsened the filter characteristics. The FWHM of the filter significantly increased due to thermal annealing. Notably, Al sublimation begins around 190 degrees Celsius, with a melting point of approximately 660 degrees Celsius (69). At the annealing temperatures used, significant Al metal sublimation occurs, and the separated metal atoms contribute to the increased transparency of the filter structure (as seen in Figure 10). Visually, the filter's transition to a nearly semi-transparent state after annealing was also discernible to the naked eye.

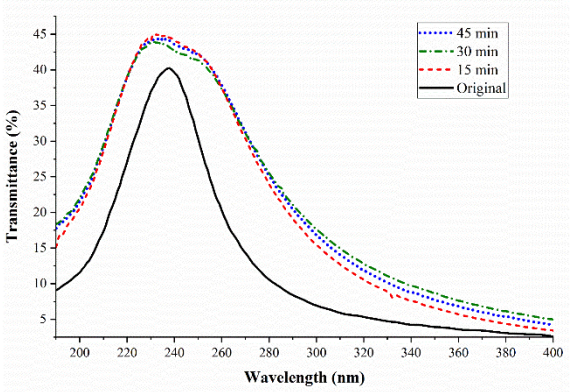

Figure 10. Effect of thermal annealing at 400 degrees Celsius for 15, 30, and 45 minutes on the optical transmittance spectrum of the bandpass filter.

Laser damage threshold measurement is a used method for assessing the stability and durability of deposited layers in the UV region (61). There are also reports on using this method to measure the damage threshold of bandpass optical filters (70, 71). Based on these reports, the laser damage threshold of the prepared bandpass filters was measured in this study. The measurements were performed using a Nd:YAG laser at a fundamental wavelength of 1064 nm, with a pulse energy of 150 mJ and a pulse width of 10 ns (see Figure 11). The measurements followed ISO 11254 guidelines using the one-on-one method (72). The laser energy was tuned by a polarizer, and a half-wave plate provided linear polarization. The lens focused the beam on the sample surface enclosed within a safety chamber. A two-axis microstage scanned the sample in the laser beam focus, monitored by a computer-controlled CCD. A beamsplitter directed a portion of the laser beam to the laser energy meter. The determined damage threshold for the samples was approximately 1.3 J/cm². The laser damage threshold was measured at the fundamental wavelength of the Nd:YAG laser (1064 nm, 10 ns pulse width) following ISO 11254 guidelines. While this value provides a useful indicator of the overall mechanical and thermal durability of the multilayer stack, it should be noted that the damage threshold at the operational wavelength of 222 nm is expected to be lower due to the significantly higher photon energy (~5.6 eV vs. ~1.17 eV at 1064 nm), which increases the likelihood of photochemical and multiphoton absorption processes in the dielectric and metal layers. Nevertheless, the 1064 nm measurement serves as a standard proxy for coating robustness in UV applications, consistent with common practice in thin-film optics characterization.

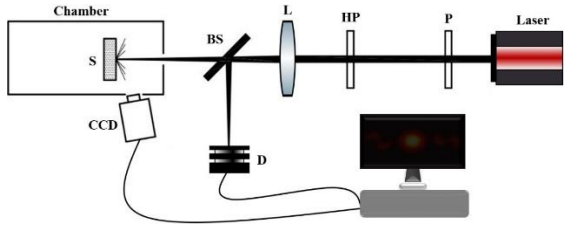

Figure 11. Schematic of the used optical setup for laser damage threshold measurements.

Discussion

A critical design consideration is the trade-off between peak transmittance and the FWHM. While increasing the peak transmittance is desirable, it inherently comes at the cost of a larger FWHM, which can lead to the transmission of unsafe, longer UVC wavelengths. Additionally, the skin depth of aluminum at 222 nm is approximately 8.9 nm. Therefore, selecting a single aluminum layer thicker than this value is essential to ensure minimal light transmission in the visible wavelength range.

Experimental fabrication revealed deviations from the theoretical design, as the first fabricated sample exhibited a transmission peak at 247 nm instead of the targeted 222 nm. These discrepancies stem from errors encountered during the transition from the design to the fabrication phase, primarily due to differences between the designed layer thicknesses and the actual thicknesses achieved during deposition. Such inaccuracies often result from thickness measurement errors, as quartz crystal microbalances in deposition systems require careful recalibration and eventual replacement after prolonged use.

To quantify these fabrication tolerances, linear sensitivity analysis and error modeling were performed. Modeling indicated that a ±1 nm error in MgF_2 layer thickness results in a dominant peak wavelength shift of approximately ±3.2 nm, primarily due to changes in the optical path length of the dielectric layers. In contrast, a similar error in Al layer thickness causes a much smaller shift (~±0.4 nm), mainly impacting peak transmittance due to increased absorption and scattering in thicker metal layers. Thus, the observed red-shift in the first sample was primarily attributed to deposition errors in the MgF_2 layers. Additionally, physical vapor deposition of MgF_2 at room temperature can result in film porosity due to limited adatom mobility, which typically leads to lower effective refractive indices and would theoretically favor a blue-shift. However, the adsorption of atmospheric moisture into these pores can temporarily increase the effective refractive index, potentially contributing a minor red-shift component (estimated <5 nm) that partially explains the observed spectral shift.

While post-deposition thermal annealing is a well-known technique to correct structural defects and enhance optical properties, it proved detrimental to the fabricated filters. Subjecting the sample to 400 °C worsened the filter characteristics and significantly increased the FWHM. This failure is attributed to the thermal instability of the metal layer; aluminum sublimation begins around 190 °C. At the applied annealing temperatures, significant aluminum sublimation occurred, separating metal atoms and visibly transitioning the filter to a nearly semi-transparent state.

Finally, the laser damage threshold was measured at approximately 1.3 J/cm² using a 1064 nm Nd:YAG laser. While this 1064 nm measurement serves as a standard proxy for evaluating the overall mechanical and thermal robustness of the multilayer stack, the damage threshold at the operational wavelength of 222 nm is expected to be lower. The significantly higher photon energy at 222 nm (~5.6 eV compared to ~1.17 eV at 1064 nm) increases the likelihood of photochemical and multiphoton absorption processes within the dielectric and metal layers.

Conclusion

In this study, we have delved into the intricate realm of optical bandpass filters designed specifically for the generation of 222 nm UVC light—a wavelength crucial for effective sterilization while minimizing harm to human health. Our exploration spanned critical aspects,

including material selection, layer thickness optimization, and rigorous experimental fabrication and characterization of the metal-dielectric 222 nm bandpass filters. Our investigation into cost-effective designs, ensures that their practical implementations remain economically viable. Several optimal designs for 222 nm optical bandpass filters were presented, providing users with different options. Depending on material availability and desired filter characteristics, users can then choose the most suitable design.

The successful development of efficient 222 nm UVC light sources holds immense promise for healthcare facilities, public spaces, and personal protective equipment. These filters can play a pivotal role in mitigating the spread of infectious diseases, including the recent pandemics. Exploring novel dielectric materials beyond MgF_2 and the other provided designs in this study can further enhance the filter performance. Furthermore, integrating these filters into existing UVC devices or designing portable UVC light sources for personal protection warrants further exploration.

Acknowledgment

This study was funded by a project grant from the Iranian National Scientific Foundation (INSF; contract No. 99010572).

References

1. Lomaev MI, Sosnin EA, Tarasenko VF. Excilamps and their applications. Progress in quantum electronics. 2012;36(1):51-97.
2. Van der Schans M, Yu J, de Vries A, Martin G. Estimation of the UV susceptibility of aerosolized SARS-CoV-2 to 254 nm irradiation using CFD-based room disinfection simulations. Scientific Reports. 2024;14(1):15963.
3. Monika, Madugula SK, Kondabagil K, Kunwar A. Far-UVC (222 nm) irradiation effectively inactivates ssRNA, dsRNA, ssDNA, and dsDNA viruses as compared to germicidal UVC (254 nm). Photochemistry and Photobiology.
4. Tavares RSN, Adamoski D, Girasole A, Lima EN, da Silva Justo-Junior A, Domingues R, et al. Different biological effects of exposure to far-UVC (222 nm) and near-UVC (254 nm) irradiation. Journal of Photochemistry and Photobiology B: Biology. 2023;243:112713.
5. Sugihara K, Kaidzu S, Sasaki M, Ichioka S, Takayanagi Y, Shimizu H, et al. One-year ocular safety observation of workers and estimations of microorganism inactivation efficacy in the room irradiated with 222-nm far ultraviolet-C lamps. Photochemistry and Photobiology. 2023;99(3):967-74.
6. Welch D, Kleiman NJ, Arden PC, Kuryla CL, Buonanno M, Ponnaiya B, et al. No evidence of induced skin cancer or other skin abnormalities after long-term (66 week) chronic exposure to 222-nm far-UVC radiation. Photochemistry and photobiology. 2023;99(1):168-75.
7. Ma B, Bright K, Ikner L, Ley C, Seyedi S, Gerba CP, et al. UV inactivation of common pathogens and surrogates under 222 nm irradiation from KrCl* excimer lamps. Photochemistry and Photobiology. 2023;99(3):975-82.
8. Sharif S, Mozaffari-Jovin S, Alizadeh F, Mojarrad M, Baharvand H, Nouri M, et al. Isolation of plasma small extracellular vesicles by an optimized size-exclusion chromatography-based method for clinical applications. Journal of Drug Delivery Science and Technology. 2023;87:104796.
9. Khorshid Sokhangouy S, Alizadeh F, Lotfi M, Sharif S, Ashouri A, Yoosefi Y, et al. Recent advances in CRISPR-Cas systems for colorectal cancer research and therapeutics. Expert Review of Molecular Diagnostics. 2024;24(8):677-702.
10. Barber VP, Goss MB, Franco Deloya LJ, LeMar LN, Li Y, Helstrom E, et al. Indoor Air Quality Implications of Germicidal 222 nm Light. Environmental Science & Technology. 2023.
11. Welch D, Buonanno M, Grilj V, Shuryak I, Crickmore C, Bigelow AW, et al. Far-UVC light: A new tool to control the spread of airborne-mediated microbial diseases. Scientific Reports. 2018;8(1):2752.
12. Buonanno M, Kleiman NJ, Welch D, Hashmi R, Shuryak I, Brenner DJ. 222 nm far-UVC light markedly reduces the level of infectious airborne virus in an occupied room. Scientific Reports. 2024;14(1):6722.
13. Song B-M, Lee G-H, Han H-J, Yang J-H, Lee E-G, Gu H, et al. Ultraviolet-C light at 222 nm has a high disinfecting spectrum in environments contaminated by infectious pathogens, including SARS-CoV-2. Plos one. 2023;18(11):e0294427.
14. Blatchley III ER, Brenner DJ, Claus H, Cowan TE, Linden KG, Liu Y, et al. Far UV-C radiation: An emerging tool for pandemic control. Critical Reviews in Environmental Science and Technology. 2023;53(6):733-53.
15. Sargent R, Sytchkova A, Jensen L. Optical Interference Coatings 2022: introduction to the feature issue. Applied Optics. 2023;62(7):OIC1-OIC5.
16. Madsen C. Efficient architectures for exactly realizing optical filters with optimum bandpass designs. IEEE Photonics technology letters. 1998;10(8):1136-8.
17. Niraula M, Yoon JW, Magnusson R. Single-layer optical bandpass filter technology. Optics Letters. 2015;40(21):5062-5.
18. Dashti M, Emami F, Zohoori S. Advancements in the design and optimization of plasmonic bandpass filters for enhanced optical communication systems: a comprehensive review. Discover Electronics. 2024;1(1):10.
19. Zhang Y, Wang Y, Zhang R, editors. Improved Lidar system based on optical bandpass filter. Optical Sensing and Imaging Technologies and Applications; 2018: SPIE.
20. Perez G, Genova I, Alvarado CG, Sanz JM, editors. Design, preparation, and characterization of high-performance narrow-bandpass filters for the infrared range. Advances in Optical Thin Films; 2004: SPIE.
21. Macleod HA. Thin-film optical filters. Boca Raton, FL: CRC Press; 2017.
22. Nishigori C, Yamano N, Kunisada M, Nishiaki-Sawada A, Ohashi H, Igarashi T. Biological impact of shorter wavelength ultraviolet radiation-C.

Photochemistry and Photobiology. 2023;99(2):335-43.
23. Welch D, Buonanno M, Shuryak I, Randers-Pehrson G, Spotnitz HM, Brenner DJ, editors. Far-UVC light applications: sterilization of MRSA on a surface and inactivation of aerosolized influenza virus. Light-Based Diagnosis and Treatment of Infectious Diseases; 2018: SPIE.
24. Ma B, Gundy PM, Gerba CP, Sobsey MD, Linden KG. UV inactivation of SARS-CoV-2 across the UVC spectrum: KrCl* excimer, mercury-vapor, and light-emitting-diode (LED) sources. Applied and environmental microbiology. 2021;87(22):e01532-21.
25. Panzures A. 222-nm UVC light as a skin-safe solution to antimicrobial resistance in acute hospital settings with a particular focus on methicillin-resistant Staphylococcus aureus and surgical site infections: a review. Journal of Applied Microbiology. 2023;134(3):lxad046.
26. Narita K, Asano K, Yamane K, Ohashi H, Igarashi T, Nakane A. Effect of ultraviolet C emitted from KrCl excimer lamp with or without bandpass filter to mouse epidermis. Plos one. 2022;17(5):e0267957.
27. Brantner C, Wong A, Davis A, Hammond C, Olson N. Safety of 222 Nm Band-Pass Filtered Irradiation: A Review and Analysis of Current Data. Boeing; 2020.
28. Eadie E, O'Mahoney P, Ibbotson SH, Miller CC, Wood K. Far-UVC: The impact of optical filters on real-world deployment. Photochemistry and Photobiology. 2024.
29. Ohashi H, Koi T, Igarashi T. State-of-the-art Technology: Inactivation of Pathogens Using a 222-nm Ultraviolet Light Source with an Optical Filter. Journal of Science and Technology in Lighting. 2021;44(0):9-11.
30. Zeinali M, Jaleh B, Vaziri MR, Omidvar A. Study of nonlinear optical properties of TiO2−polystyrene nanocomposite films. Quantum Electronics. 2019;49(10):951.
31. Vaziri MR, Hajiesmaeilbaigi F. Optical and structural properties of copper nanostructured thin films prepared by pulsed laser deposition. Optik. 2015;126(14):1348-51.
32. Vaziri MR. Describing the propagation of intense laser pulses in nonlinear Kerr media using the ducting model. Laser Physics. 2013;23(10):105401.
33. Vaziri MR, Hajiesmaeilbaigi F, Maleki MH. New ducting model for analyzing the Gaussian beam propagation in nonlinear Kerr media and its application to spatial self-phase modulations. Journal of Optics. 2013;15(3):035202.
34. Beigzadeh AM, Vaziri MR. Z-scan dosimetry of gamma-irradiated PMMA. Nuclear Instruments and Methods in Physics Research Section A: Accelerators, Spectrometers, Detectors and Associated Equipment. 2021;991:165022.
35. Beigzadeh AM, Rashidian Vaziri MR, Ziaie F, Sharif S. A new optical method for online monitoring of the light dose and dose profile in photodynamic therapy. Lasers in surgery and medicine. 2020;52(7):659-70.
36. Beigzadeh AM, Vaziri MR, Ziaie F, Soltani Z. Double-exposure holographic interferometry for radiation dosimetry: A new developed model. Radiation Measurements. 2018;119:132-9.
37. Bloemer MJ, Scalora M. Transmissive properties of Ag/MgF 2 photonic band gaps. Applied Physics Letters. 1998;72(14):1676-8.
38. Jakšić Z, Maksimović M, Sarajlić M. Silver–silica transparent metal structures as bandpass filters for the ultraviolet range. Journal of Optics A: Pure and Applied Optics. 2004;7(1):51.
39. Mu J, Lin P-T, Zhang L, Michel J, Kimerling L, Jaworski F, et al. Design and fabrication of a high transmissivity metal-dielectric ultraviolet band-pass filter. Applied Physics Letters. 2013;102(21):213105.
40. Austin R. The Use of Solid Etalon Devices as Narrow Band Interference Filters. Optical Engineering. 1972;11(3):110365.
41. Rust D. Étalon filters. Optical Engineering. 1994;33(10).
42. Su G, Zhuang X, He Y, Zheng G. A new crystal of ammonium cobalt nickel sulfate hexahydrate for UV light band-pass filter. Optical Materials. 2008;30:916-9.
43. Thirupathy J, Sahaya Jude Dhas S, Jose M, Dhas SAMB. An investigation on optical, mechanical and thermal properties of nickel sulphate hexahydrate single crystal—a UV band pass filter. Materials Research Express. 2019;6(8):086206.
44. Khayyat N, Dizaji H. Growth of K2Ni(SO4)2.6H2O crystal by Sankaranarayanan-Ramsamy (SR) method for UV light band-pass filter. Optik - International Journal for Light and Electron Optics. 2015;126.
45. Zhu J, Nakakubo K, Mikami Y, Yoshioka H, Morita K, Oki Y. Investigation and modeling of UV band-pass-filtering white compound materials for potting or embedding in micro-optical applications. Optical Materials Express. 2019;9(3):1002-14.
46. Kedawat G, Gupta BK, Kumar P, Dwivedi J, Kumar A, Agrawal NK, et al. Fabrication of a flexible UV band-pass filter using surface plasmon metal-polymer nanocomposite films for promising laser applications. ACS Appl Mater Interfaces. 2014;6(11):8407-14.
47. Kim S, Man M, Qi M, Webb KJ. Angle-insensitive and solar-blind ultraviolet bandpass filter. Opt Lett. 2014;39(19):5784-7.
48. Li W-D, Chou SY. Solar-blind deep-UV band-pass filter (250 - 350 nm) consisting of a metal nano-grid fabricated by nanoimprint lithography. Opt Express. 2010;18(2):931-7.
49. Dai J, Wang G, Liu B, Cao X, Tao T, Xie ZL, et al. Design and fabrication of UV band-pass filters based on SiO2/Si3N4 dielectric distributed bragg reflectors. Applied Surface Science. 2016;364:886-91.
50. Yang Y, Bai Y, Zhao X, Zhang M, Fei H, Chen Z. Design of a solar-blind ultraviolet band-pass filter based on frequency domain superposition. Superlattices and Microstructures. 2018;122:486-91.
51. Ockenfuss G, editor Metal-oxide Ultraviolet Narrow-band-pass Filter at 214 nm. Optical Interference Coatings; 2013 2013/06/16; Whistler: Optica Publishing Group.
52. Guan H, Han P, Li Y, Zhang X, Zhang W. Analysis and optimization of a new photonic crystal filters in near ultraviolet band. Optik. 2012;123:1874-8.

53. Ikematsu T, Hayashi N, Ihara S, Satoh S, Yamabe C. Advanced oxidation processes (AOPs) assisted by excimer lamp. Vacuum. 2004;73(3-4):579-82.
54. Robinson RT, Mahfooz N, Rosas-Mejia O, Liu Y, Hull NM. SARS-CoV-2 disinfection in aqueous solution by UV₂₂₂ from a krypton chlorine excilamp. medRxiv. 2021:2021.02.19.21252101.
55. Liu B, Mullen L, Payne E, Linden K. Accelerated Ultraviolet Treatment of Carbamazepine and NDMA in Water under 222 nm Irradiation. Environmental science & technology. 2023;57.
56. Suzuki N, Okazaki A, Kuriyama H, Serizawa I, Hara A, Hirano Y, et al. Synthesis of Mesoporous TiO2/Boron-Doped Diamond Photocatalyst and Its Photocatalytic Activity under Deep UV Light (λ = 222 nm) Irradiation. Molecules. 2018;23:3095.
57. Sarangan A. Transfer Matrix Method. Optical Thin Film Design: CRC Press; 2020. p. 49-63.
58. Katsidis CC, Siapkas DI. General transfer-matrix method for optical multilayer systems with coherent, partially coherent, and incoherent interference. Applied optics. 2002;41(19):3978-87.
59. Gerrard A, Burch JM. Introduction to matrix methods in optics: Courier Corporation; 1994.
60. Macleod A, Clark C. Optical coating design with the Essential Macleod. 2012.
61. Rainer F, Lowdermilk WH, Milam D, Carniglia CK, Hart TT, Lichtenstein TL. Materials for optical coatings in the ultraviolet. Applied optics. 1985;24(4):496-500.
62. Ehrenreich H, Philipp H, Segall B. Optical properties of aluminum. Physical Review. 1963;132(5):1918.
63. Scalora M, Bloemer M, Pethel A, Dowling J, Bowden C, Manka A. Transparent, metallo-dielectric, one-dimensional, photonic band-gap structures. Journal of Applied Physics. 1998;83(5):2377-83.
64. Cheng F, Su P-H, Choi J, Gwo S, Li X, Shih C-K. Epitaxial growth of atomically smooth aluminum on silicon and its intrinsic optical properties. ACS nano. 2016;10(11):9852-60.
65. Kitamura R, Pilon L, Jonasz M. Optical constants of silica glass from extreme ultraviolet to far infrared at near room temperature. Applied optics. 2007;46(33):8118-33.
66. Liang R, Wang H, Zhan S, Ye M, Shu L, Fei L, et al. High-temperature flexible transparent heater for rapid thermal annealing of thin films. Physical Review Applied. 2022;17(4):044049.
67. Li Z-W, Chen S-T, Ho M-F, Young S-L. Post thermal annealing effect on optical properties of a-Si: H/SiO 2 multilayer thin films for Bandpass Filter. Int J Latest Trans Eng Sci. 2021;12(1):5-13.
68. Kumar SA, Nagendra C, Shanbhogue HG, Thutupalli G. Near-infrared bandpass filters from Si/SiO2 multilayer coatings. Optical Engineering. 1999;38(2):368-80.
69. Jones F, Wood K. The melting point of thin aluminium films. British journal of applied physics. 1964;15(2):185.
70. Zhu Z, Cheng X, Xu Z, Huang L, Liu Z. Wavelength dependent damage thresholds of a bandpass filter under femtosecond laser irradiation. Applied Physics A. 2013;111:1091-8.
71. Callahan GP, Flint BK, editors. Characteristics of deep-UV optics at 193 nm and 157 nm. Laser-Induced Damage in Optical Materials: 1998; 1999: SPIE.
72. Becker J, Bernhardt A, editors. ISO 11254: an international standard for the determination of the laser-induced damage threshold. Laser-Induced Damage in Optical Materials: 1993; 1994: SPIE.